

# In-Plane Transport Properties of Si/Si<sub>1-x</sub>Ge<sub>x</sub> Structure and its FET Performance by Computer Simulation

Toshishige Yamada, *Member, IEEE*, Jing-Rong Zhou, *Member, IEEE*,  
H. Miyata, and David K. Ferry, *Fellow, IEEE*

**Abstract**—Transport properties of ungated Si/Si<sub>1-x</sub>Ge<sub>x</sub> are studied by an ensemble Monte Carlo technique. The device performance is studied with a quantum hydrodynamic equation method using the Monte Carlo results. The phonon-scattering-limited mobility is enhanced over bulk Si, and is found to reach 23000 cm<sup>2</sup>/Vs at 77 K and 4000 cm<sup>2</sup>/Vs at 300 K. The saturation velocity is increased slightly compared with the bulk value at both temperatures. A significant velocity overshoot, several times larger than the saturation velocity, is also found. In a typical modulation-doped field-effect-transistor, the calculated transconductance for a 0.18 μm gate device is found to be 300 mS/mm at 300 K. Velocity overshoot in the strained Si channel is observed, and is an important contribution to the transconductance. The inclusion of the quantum correction increases the total current by as much as 15%.

## I. INTRODUCTION

THERE has been significant progress in efforts to achieve high electron mobility in a modulation-doped, strained Si layer grown on a relaxed Si<sub>1-x</sub>Ge<sub>x</sub> substrate [1]–[4]. Experimentally observed mobility values typically are 175000 cm<sup>2</sup>/Vs below 4.2 K, 9500 cm<sup>2</sup>/Vs at 77 K, and 1600 cm<sup>2</sup>/Vs at 300 K [1]–[3], which are well above those of bulk Si, and exhibit a profound potential for device applications. In fact, a high-transconductance n-type Si/Si<sub>1-x</sub>Ge<sub>x</sub> modulation-doped field-effect transistor (FET) has been created [3] with 600 mS/mm at 77 K for a gate length of 0.25 μm. In this Si/Si<sub>1-x</sub>Ge<sub>x</sub> system, a two-dimensional (2D) electron gas is created in the strained Si (100) layer, which is grown on a relaxed Si<sub>1-x</sub>Ge<sub>x</sub> (100) substrate. Once the heterojunction is formed, the strain at the interface causes the six-fold degenerate  $\Delta$  valleys in Si to split into two groups: two lowered valleys that exhibit the longitudinal mass normal to the heterointerface, and four raised valleys that have the longitudinal mass parallel to the interface [4]. The conduction band formed by the lowered valleys is now lower than that of Si<sub>1-x</sub>Ge<sub>x</sub> and the band alignment across the heterojunction creates a potential barrier for electrons, so that a type II

superlattice is formed [4]. The electrons prefer to populate the lowered valleys, which are energetically favored.

The splitting energy between lowered and raised valleys,  $\Delta E$ , is empirically represented by 0.6x eV, where x is the Ge fraction in the Si<sub>1-x</sub>Ge<sub>x</sub> substrate [4]. The standard choice of x = 0.3 [1]–[3] gives a valley splitting energy as large as 0.18 eV, which is one order of magnitude larger than the thermal energy, even at room temperature. This wide splitting is expected to suppress the intervalley phonon scattering of electrons from the lowered valleys to the raised valleys, and effectively reduces the intervalley phonon scattering rate compared with that of unstrained Si. In the lowered valleys, electrons show the smaller transverse mass  $m_t$  in transport parallel to the interface. These two factors are considered to be the main mechanisms for the high mobility and the high transconductance in the devices above [3]. The strain also causes a change in the bandgap  $E_g$ , which is empirically given by  $E_g(x) = 1.11 - 0.4x$  eV [4]. This affects impact ionization and changes the high field transport properties as well.

We have adopted an ensemble Monte Carlo technique to study the transport property of an ungated strained Si layer assumed to be grown on a relaxed Si<sub>1-x</sub>Ge<sub>x</sub> substrate, and then used a quantum-hydrodynamic-equation (QHE) method [5] to study a modulation-doped Si/Si<sub>1-x</sub>Ge<sub>x</sub> FET structure. In principle, the present Monte Carlo model is based on that of the usual unstrained bulk Si [6], and the effect of Si/Si<sub>1-x</sub>Ge<sub>x</sub> heterojunction formation is included in the band structure that is modified by the strain at the heterojunction [7]. Our basic bulk-Si Monte Carlo model is a little different from others, in that we have introduced first order *f*- and *g*-phonon scattering [6], and this is discussed in detail in the Appendix. The Monte Carlo simulation gives the velocity-field and energy-field characteristics of an ungated Si/Si<sub>1-x</sub>Ge<sub>x</sub> structure, and these results are used as input data for the QHE method, which simulates electron transport in a gated FET structure in a hydrodynamic picture, including the quantization effect of electrons as a quantum potential term in the equations [5].

It is found that the phonon-scattering-limited mobility is enhanced greatly, 23000 cm<sup>2</sup>/Vs at 77 K and 4000 cm<sup>2</sup>/Vs at 300 K, and the saturation velocity is increased slightly compared with the bulk value at both temperatures. A significant velocity overshoot is also found. In a Si/Si<sub>1-x</sub>Ge<sub>x</sub> FET structure at 300 K, the calculated transconductance is about 300 mS/mm. Velocity overshoot in the strained Si channel is observed,

Manuscript received November 8, 1993; revised May 31, 1994. The review of this paper was arranged by Associate Editor A. H. Marshak. This work supported in part by the Office of Naval Research and the Army Research Office.

T. Yamada, J.-R. Zhou, and D. K. Ferry are with the Center for Solid State Electronics Research, Arizona State University, Tempe, AZ 85287-6206 USA. H. Miyata is with Fujitsu Ltd., Kawasaki, Japan.  
IEEE Log Number 9403887.

which is several times faster than the saturation velocity. The device performances are discussed in comparison with those of other FET models, such as AlGaAs/GaAs HEMT.

In Section II, the Monte Carlo model and the QHE method are briefly explained. The simulation results are presented in Section III and conclusions are given in Section IV. The Appendix explains our unstrained bulk Si Monte Carlo model, which is the basis of the simulations (77 and 300 K) in this paper.

## II. SIMULATION MODEL

### A. Monte Carlo Model for Ungated Structure at 77 and 300 K

In a strained Si channel of a modulation-doped structure whose conduction-band diagram is shown in Fig. 1, the effect of strain is included only in the band structure as the valley splitting energy  $\Delta E$  [7]. (In the modulation-doped heterostructure, it is known that quantization in the channel adds to the valley splitting [8], so that we use this simple parameter to characterize the layer.) The effective masses of the electrons are assumed to be unchanged [9]. The conduction band structure is modeled in a simple manner, with a nonparabolic-band model within the effective mass approximation. This is justified if we are interested in transport phenomena below  $\sim 5 \times 10^5$  V/cm, and are not interested in the detailed shape in the high energy tail of the energy distribution function. This will be discussed in detail with the simulation results for the distribution function at high fields. The 2D nature of the scattering in the quantized layer is neglected for this high temperature region of 77–300 K [7], where we are particularly interested in the high field properties. In order to model the smaller transverse-mass transport properly, the explicit inclusion of the longitudinal and transverse masses is important and this is done in the Monte Carlo program using the Herring–Vogt transformation [10] with a three-valley model: lowered valley pair 1 is in the (100) direction, raised valley pair 2 is in the (010) direction, and raised valley pair 2 is in the (001) direction, with the electric field in the (001) direction. We use zeroth-order  $f$ - and  $g$ -phonons and first-order  $f$ - and  $g$ -phonons for intervalley scattering [6] as well as acoustic phonons. The various phonon coupling constants are assumed to be the same as unstrained Si [9], and a usual set of coupling constants for the phonon modes discussed in the Appendix is adopted, which recovers the measured velocity-field characteristics reported in [11] and other relevant experimental results. We assume that the strained Si channel does not contain background impurities and the spacer is thick enough that ionized impurity scattering does not play an important role. Impact ionization is important in the strained Si channel because of the bandgap reduction, and is included for the study of higher fields with a soft ionization model by Ridley [12]. According to this soft model, the impact-ionization scattering rate is a quadratic function of electron kinetic energy above the ionization threshold energy  $E_{th}$ . The threshold energy  $E_{th}$  of strained Si is assumed to be proportional to the bandgap, by  $E_{th}(x) = 1.18E_g(x)/E_g(0)$ .

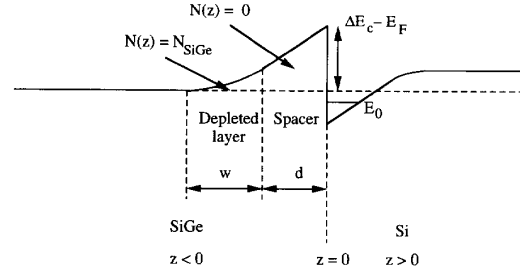


Fig. 1. Energy band structure of Si/Si<sub>1-x</sub>Ge<sub>x</sub> across the heterointerface.

When ionization occurs, the original electron loses kinetic energy equal to  $E_g(x)$ . The original electrons are assumed to not change valley during ionization. Nonparabolicity is also important in strained Si, since the nonparabolicity parameter  $\alpha$  is inversely proportional to the bandgap  $E_g(x)$ , and is included in the simulation. In the Appendix, the bulk Si Monte Carlo model is explained in more detail, as the basis for our present program for strained Si.

### B. Quantum Hydrodynamic Equation Model for Device Simulation

A set of quantum hydrodynamic equations is used in the simulation. The equations, which explicitly include quantum corrections and describe the particle conservation, momentum conservation, and energy conservation, are discussed in detail in [5]. We restate the equations as follows:

$$\frac{\partial n}{\partial t} + \nabla \cdot (n\mathbf{v}) = 0 \quad (1)$$

$$\frac{\partial \mathbf{v}}{\partial t} + \mathbf{v} \cdot \nabla \mathbf{v} = -\frac{q\mathbf{E}}{m^*} - \frac{1}{nm^*} \nabla (nk_B T_q) - \frac{\mathbf{v}}{\tau_m} \quad (2)$$

$$\frac{\partial T}{\partial t} + \frac{1}{3\gamma} \mathbf{v} \cdot \nabla (T_q) = -\frac{2}{3\gamma} \nabla \cdot (\mathbf{v} T_q) + \frac{m^* \mathbf{v}^2}{3\gamma k_B} \cdot \left( \frac{2}{\tau_m} - \frac{1}{\tau_w} \right) - \frac{T - T_0}{\tau_w} \quad (3)$$

where  $n$  is the average electron density,  $\mathbf{v}$  is the average electron velocity,  $T$  is the effective electron temperature,  $m^*$  is the effective electron mass,  $\mathbf{E}$  is the electric field,  $\tau_m$  is the momentum relaxation time,  $\tau_w$  is the energy relaxation time,  $T_0$  is the lattice temperature, and  $T_q$  is given by

$$T_q = \gamma T + \frac{2}{3k_B} U_q \quad (4)$$

with

$$U_q = \frac{-\hbar^2}{8m^*} \nabla^2 \ln(n) \quad (5)$$

where the  $U_q$  is the quantum correction. The explicit quantum correction involves the second order space derivative of the log density. Thus the correction tends to smooth the electron distribution, especially where the electron density has sharp change, e.g., when approaching a sharp potential barrier. The factor  $\gamma$  in (4) is the degeneracy factor [14]

$$\gamma = \gamma(\mu_f/k_B T) = \frac{F_{3/2}(\mu_f/k_B T)}{F_{1/2}(\mu_f/k_B T)} \quad (6)$$

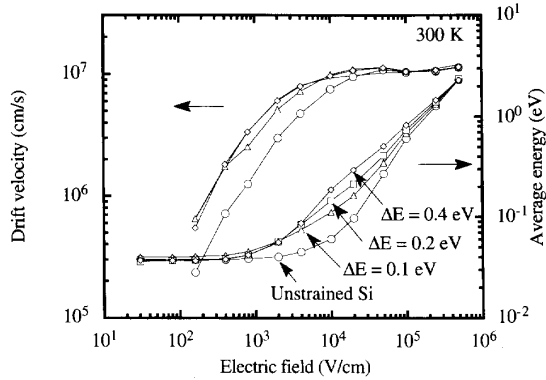


Fig. 2. Velocity-field and energy-field characteristics of an electron in a strained Si layer for various valley splitting values  $\Delta E$ , where unstrained Si corresponds to  $\Delta E = 0$  at 300 K. The symbol corresponding to each value of  $\Delta E$  is consistent throughout this paper: circle for unstrained Si ( $\Delta E = 0$ ), triangle for  $\Delta E = 0.1$  eV, square for  $\Delta E = 0.2$  eV, and diamond for  $\Delta E = 0.4$  eV.

where  $F_j$  is the Fermi-Dirac integral, and  $\mu_f$  is the Fermi energy measured from the conduction band edge. The factor  $\gamma$  is introduced as a correction to the total average electron kinetic energy (assuming a Fermi-Dirac distribution function):

$$w = \frac{1}{2}m^*v^2 + \frac{3}{2}\gamma k_B T + U_q. \quad (7)$$

The relaxation times  $\tau_m$  and  $\tau_w$ , which are functions of energy, are determined by fitting the homogeneous hydrodynamic equations to the velocity-field and energy-field relations from Monte Carlo simulation.

### III. RESULTS AND DISCUSSION

#### A. High-Field Transport

Fig. 2 shows the velocity-field and energy-field characteristics at 300 K for several valley splitting values  $\Delta E = 0, 0.1, 0.2,$  and  $0.4$  eV where “unstrained Si” indicates the characteristics of  $\Delta E = 0$ . The characteristics do not show a significant difference for strained Si with  $\Delta E \gtrsim 0.1$  eV, so we can categorize unstrained and strained Si. The mobility for strained Si is almost triple in low fields,  $4000 \text{ cm}^2/\text{Vs}$ , that of unstrained Si,  $1500 \text{ cm}^2/\text{Vs}$ , due to the smaller transverse-mass transport. In fields larger than  $20 \text{ kV/cm}$ , all curves approach one another and have a similar saturation velocity  $\sim 1.0 \times 10^7 \text{ cm/s}$  at 300 K, although strained Si tends to show a slightly higher value. The mobility is higher at 77 K,  $17000 \text{ cm}^2/\text{Vs}$  for unstrained Si, and  $23000 \text{ cm}^2/\text{Vs}$  for strained Si, respectively, and the saturation velocity is reached for fields larger than  $\sim 5 \text{ kV/cm}$ . Again, there is no significant difference between them, although strained Si tends to show a slightly higher value. The saturation velocity is estimated to be  $\sim 1.3 \times 10^7 \text{ cm/s}$  at 77 K.

The energy origin is chosen at the bottom of the lowered valleys (valley pair 1 in the present model), and the average of the sum of kinetic energy and potential energy (0 in the lower valley and  $\Delta E$  in the upper valleys) is plotted in the figure. Energy at thermal equilibrium is  $3k_B T/2 = 39 \text{ meV}$  at 300 K and increases monotonically with the field. The energy

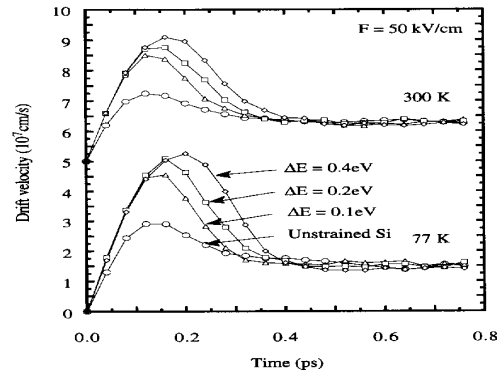


Fig. 3. Transient overshoot velocity with a sudden application of the field  $50 \text{ kV/cm}$  for various valley splitting values  $\Delta E$  at 300 and 77 K.

has a clear dependence on  $\Delta E$ , although this is lost in fields larger than  $100 \text{ kV/cm}$ . In higher fields, electrons have an energy larger than  $\Delta E$  so there is no significant difference for different  $\Delta E$ 's. It has to be noted that the impact ionization is more important as  $\Delta E$  increases, since the bandgap and therefore the threshold decrease with  $\Delta E$ . Comparing the characteristics at 77 K with the same plot at 300 K, the electron energy is smaller up to a field of  $10 \text{ kV/cm}$ , and then the order reverses in higher fields, which provides the mechanism for a larger mobility at 77 K.

The occupation in the lowest valleys for  $\Delta E = 0.1$  eV is around 90% even at 300 K and practically 100% at 77 K, due to low thermal excitation of carriers to the upper valleys in low fields ( $\gtrsim 5 \text{ kV/cm}$ ). As expected, the population equilibrates among the valleys for high fields ( $\gtrsim 100 \text{ kV/cm}$ ). The electron velocity is markedly higher when electrons are mostly in the lower valleys, in which case intervalley scattering from the lowered valleys to the raised valleys is suppressed and the smaller transverse-mass transport is realized. Unstrained Si has an equal-partition value of 33% over most of the range of the fields, unless an anisotropic electron occupation in the valleys occurs during the transport.

Fig. 3 shows the transient drift velocity when an electric field of  $50 \text{ kV/cm}$  is applied suddenly at time  $t = 0$  at 300 and 77 K. For visibility, the data for 300 K is offset by  $5 \times 10^7 \text{ cm/s}$ . The velocity shows a significant overshoot, which is enhanced with increasing  $\Delta E$ . At 300 K, the velocity reaches its steady-state value around  $t = 0.3$  to  $0.35$  ps. The peak velocity for  $\Delta E = 0.4$  eV is  $4.1 \times 10^7 \text{ cm/s}$  and the overshoot lasts for  $0.35$  ps. The product of the peak velocity and the overshoot duration time is  $\sim 0.1 \mu\text{m}$ , and this gives an estimation for the device size for which the electrons run from source to drain without reaching the steady-state velocity. This length is the same order of magnitude as the gate length of  $0.25 \mu\text{m}$  in the reported experiment [3], and their measured high transconductance can be attributed to this overshoot effect. At 77 K, the overshoot peak velocity increases again with  $\Delta E$ , and for  $\Delta E = 0.4$  eV, it is now  $5.2 \times 10^7 \text{ cm/s}$  and the transient behavior lasts for  $0.4$  ps, so that the product is larger ( $\sim 0.2 \mu\text{m}$ ). The effect of the overshoot is therefore enhanced compared with that at 300 K, and compares well with the effects in the device of [2].

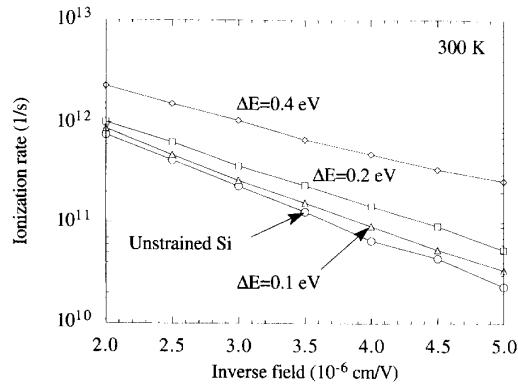


Fig. 4. Impact ionization rate of strained Si at 300 K.

Fig. 4 shows the carrier generation rate in the impact ionization process at 300 K. As expected, the ionization rate increases with increasing  $\Delta E$ , because of the reduction of the bandgap induced by the strain at the heterointerface. The ionization rate also increases with increasing field as shown in the figure, and with decreasing temperature, which is the same trend found in unstrained Si. As discussed in detail in the Appendix, our Monte Carlo model shows good agreement with the experimental ionization rates reported for unstrained Si.

The population  $n_i$  and the distribution function  $f_i$  in three valley pairs ( $i = 1, 2$ , and  $3$ ) are plotted for several  $\Delta E$ 's in Figs. 5(a) and 5(b) for  $2.5 \times 10^5$  V/cm at 300 K, where the energy is defined as the summation of the electron kinetic energy and the valley split energy  $\Delta E$ . The population is a histogram, showing the number of electrons in an energy unit cell. The distribution function is calculated by dividing  $n_i$  by the state density  $\sqrt{E_k + \alpha E_k^2} \times (1 + 2\alpha E_k)$ , where  $\alpha$  is the nonparabolicity parameter and  $E_k$  is the electron kinetic energy. For clarity, the population and distribution function curves are offset for different  $\Delta E$ . The solid lines represent valley pair 1 (lowered valleys) and valley pair 2 (raised valleys) normal to the field, and the dotted line represents valley pair 3 (raised valleys) parallel to the field. The distribution functions are shown in arbitrary units, since the Pauli exclusion principle is irrelevant in the present situation and the change in the electron density simply causes a constant shift in the figure. By the symmetry, the curves for valleys normal to the field (valley pairs 1 and 2) are the same for  $\Delta E = 0$ . However, if  $\Delta E \gtrsim 0.1$  eV, the curves for the raised valleys (valley pairs 2 and 3) are practically the same.

The population decays rapidly, even at a high field of  $2.5 \times 10^5$  V/cm as shown in Fig. 5(a). Although we do not directly include the intervalley scattering from, to, and within  $L$  valley that lies  $E = 1.05$  eV above  $\Delta$  in unstrained Si [15] (in strained Si, this energy may generally change but still is a reference value to check since many features of the band structure do not change practically in strained Si [9]), our Monte Carlo model for unstrained Si, on which the present strained Si Monte Carlo model is based, recovers the experimental velocity-field characteristics and impact ionization rate, and also the Monte Carlo energy-field characteristics obtained

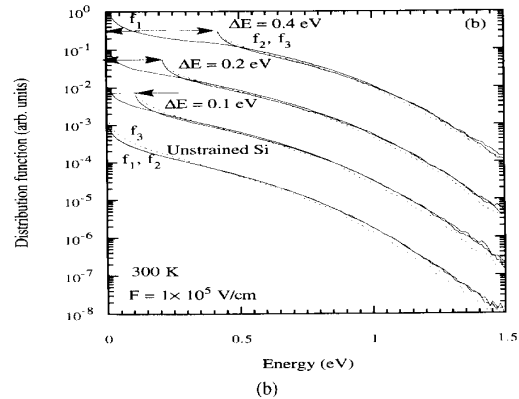
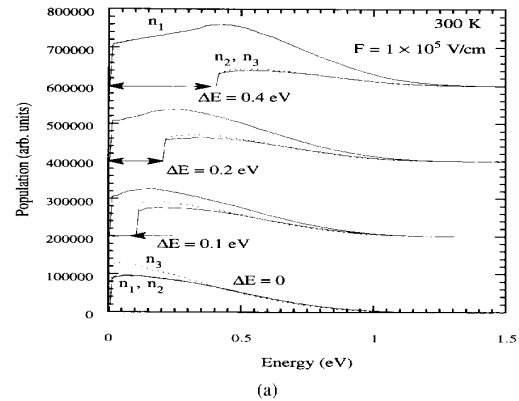


Fig. 5. (a) Population  $n_i(E)$  and (b) distribution function  $f_i(E)$  in valley pair  $i$  ( $i = 1, 2$ , or  $3$ ) for the field  $2.5 \times 10^5$  V/cm at 300 K.

with the full conduction-band model. We shall discuss this in detail in the Appendix. Above  $E = 2.38$  eV, where the conduction band for the  $\Delta$  valley has a local maximum [15] for unstrained Si, our simple nonparabolic-band approximation does not hold. The ratio of such electrons is 0.21, 0.25, 0.37, and 1.2% for  $\Delta E = 0, 0.1, 0.2$ , and  $0.4$  eV, respectively. As far as the transport properties for the fields studied here (typically  $\lesssim 5 \times 10^5$  V/cm) are concerned and the detailed shape of the distribution function for high energies ( $E \gtrsim 2.38$  eV) is out of interest, the present treatment can be justified.

We have found that the average energy increases with  $\Delta E$  in Fig. 2, and the same thing is also seen in the distribution function in Fig. 5(b). Actually, the inverse of the gradient of these curves in the high energy region is a measure of the electron temperature, and it is increasing with  $\Delta E$ . At high energies, the distribution function changes its gradient and decreases faster because of the influence of intervalley scattering, which was also reported before in different semiconductors [10], [16]. The downward convex shape of the distribution function near  $E = 0$  is due to impact ionization. Since the ionization threshold energy  $E_{th}$  is close to  $E_g$  ( $E_{th} = 1.18E_g$ ) in the present model, and electrons are assumed to lose energy  $E_g$  after suffering impact ionization, there is an inevitable accumulation of low energy electrons. This downward convex shape is more prominent if

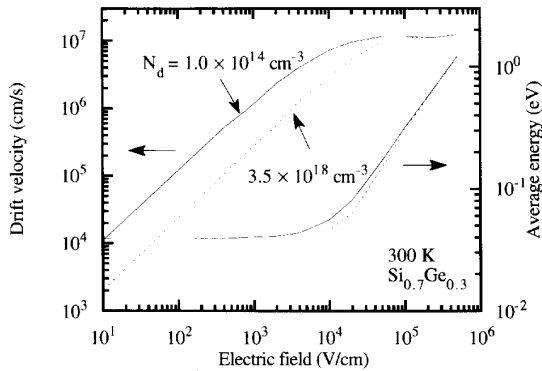


Fig. 6. Velocity-field and energy-field characteristics for  $1.5 \times 10^{18} \text{ cm}^{-3}$  doped  $\text{Si}_{0.7}\text{Ge}_{0.3}$  and  $1.0 \times 10^{14} \text{ cm}^{-3}$  doped  $\text{Si}_{0.7}\text{Ge}_{0.3}$  found from Monte Carlo simulation.

the impact ionization is more frequent and vice versa. In fact, the distribution function at a lower field  $1 \times 10^5 \text{ V/cm}$  shown in Fig. 5(c) has weaker downward convex characteristics than that of  $2.5 \times 10^5 \text{ V/cm}$ , because of the infrequent impact ionization. Note that in both Figs. 5(b) and d(c), all the distribution functions  $f_1$ ,  $f_2$ , and  $f_3$  coincide at high energy values. During the transient period, the lowered-valley distribution function  $f_1$  is different from the raised-valley distribution functions  $f_2$  and  $f_3$  at high energy values.

Although the effect is small, we need velocity-field and energy-field characteristics of doped and undoped  $\text{Si}_x\text{Ge}_{1-x}$  for a device simulation, in addition to those of strained Si discussed above, since some electrons may traverse this barrier region rather than the strained Si channel in the modulation-doped FET structure. The simulation program is a combination of the Si and Ge Monte Carlo programs, where electrons are assumed to have Si properties in  $\Delta$  valleys and Ge properties in  $L$  valleys, and the mutual valley positions in energy space are determined by the Ge ratio  $x$ . We have chosen  $x = 0.3$  for a device simulation [3]. The ionized impurity scattering is treated using Ridley's impurity scattering model [13].

The computed velocity-field and energy-field relations are plotted in Fig. 6 for both  $1.5 \times 10^{18} \text{ cm}^{-3}$  doped  $\text{Si}_{0.7}\text{Ge}_{0.3}$  and  $1.0 \times 10^{14} \text{ cm}^{-3}$  doped  $\text{Si}_{0.7}\text{Ge}_{0.3}$  at 300 K. The velocity curves show a lower electron velocity in  $\text{Si}_{0.7}\text{Ge}_{0.3}$  than that in strained Si over the entire fields, as expected. The electron low-field mobility is around a factor of two smaller in  $1.0 \times 10^{14} \text{ cm}^{-3}$  doped  $\text{Si}_{0.7}\text{Ge}_{0.3}$ , and an order of magnitude smaller in  $1.5 \times 10^{18} \text{ cm}^{-3}$  doped  $\text{Si}_{0.7}\text{Ge}_{0.3}$ , compared with the strained Si, while the high-field saturation velocity is almost the same. The average electron energy is smaller in  $\text{Si}_{0.7}\text{Ge}_{0.3}$  than that in strained Si up to the field around  $2 \times 10^5 \text{ V/cm}$ , but is larger in higher fields, since the impact ionization is less frequent in  $\text{Si}_{0.7}\text{Ge}_{0.3}$ . The relaxation times  $\tau_m$  and  $\tau_w$  in  $\text{Si}_{0.7}\text{Ge}_{0.3}$  are obtained from these characteristics in the same way as we have done for strained Si.

### B. Device Simulation

The numerical simulation has been applied to a  $0.18 \mu\text{m}$  gate, quantum-well device with a modulation-doped structure

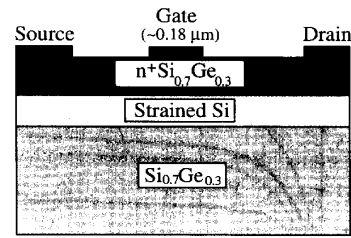


Fig. 7. Device structure.

of  $\text{Si}_{0.7}\text{Ge}_{0.3}/\text{Si}/\text{Si}_{0.7}\text{Ge}_{0.3}$ . The device structure is shown in Fig. 7. The doping of the top  $\text{Si}_{0.7}\text{Ge}_{0.3}$  layer is taken to be  $3.5 \times 10^{18} \text{ cm}^{-3}$ , and a doping of  $1.0 \times 10^{14} \text{ cm}^{-3}$  is used in the substrate  $\text{Si}_{0.7}\text{Ge}_{0.3}$ . The lattice temperature in the simulation is taken to be 300 K. The typical simulation domain is  $1.0 \mu\text{m} \times 0.095 \mu\text{m}$ . The thickness of the top  $\text{Si}_{0.7}\text{Ge}_{0.3}$  layer is 19 nm, and the strained Si channel is 18 nm. A graded interface transition is assumed for the  $\text{Si}_{0.7}\text{Ge}_{0.3}/\text{Si}$  junction which results in an effective 3 nm spacer layer. For simplicity, we only use a three-layer structure. The modulation-doped structure in [3] is more complicated. However, the active regions are similar.

The computed I-V characteristics for the  $0.18 \mu\text{m}$  gate device are shown in Fig. 8, for gate biases of 0.7, 0.5, 0.2, and 0 V, respectively. The small thickness of the top  $\text{Si}_{0.7}\text{Ge}_{0.3}$  layer provides a normally off device, since a Schottky barrier height of 0.9 V leads to an estimated depletion width of 18.4 nm. The peak transconductance is about 300 mS/mm, and good saturation with a drain conductance of 4.6 mS/mm at a gate voltage of 0.5 V is obtained. Approximately the same current level and transconductance was found in a  $0.25 \mu\text{m}$  device. The simulation results are comparable to the experimented results in [3]. The relatively larger current level ( $0.3 \text{ mA}/\mu\text{m}$ ) and transconductance (330 mS/mm) found in the experiment is thought to be due to a higher sheet density ( $2.5 \times 10^{12} \text{ cm}^{-2}$  [3] compared to  $1 \times 10^{12} \text{ cm}^{-2}$  in this simulation) in the quantum well for their particular modulation-doped structure. For comparison, we simulated an AlGaAs/GaAs HEMT with the same geometry and doping profile, this is a single heterojunction device as what we simulated before [14], which predicts a maximum transconductance of 1000 mS/mm. One could notice that the performance of the SiGe device approaches the same order of magnitude as that of the AlGaAs/GaAs device although the transconductance is a factor of three smaller.

Our simulation shows that, without including quantum corrections, the current would be 15% smaller for the  $0.18 \mu\text{m}$  gate device at a gate voltage of 0.5 V, as shown in Fig. 8. In other words, the inclusion of the quantum potential increases the total current by as much as 15% in the simulation. This large modification of the current was not expected in the device with such a gate length. However, by inspecting the density distribution along the channel, one can find that a rapid density change occurs at the gate end close to the drain

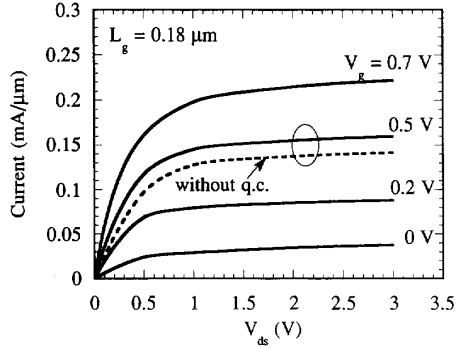
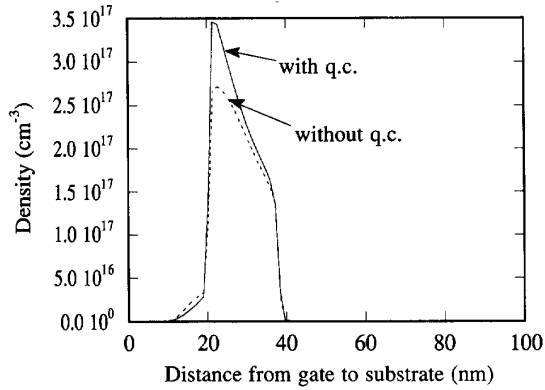
Fig. 8. I-V characteristics of a 0.18  $\mu\text{m}$  SiGe device.

Fig. 9. Electron density across the channel.

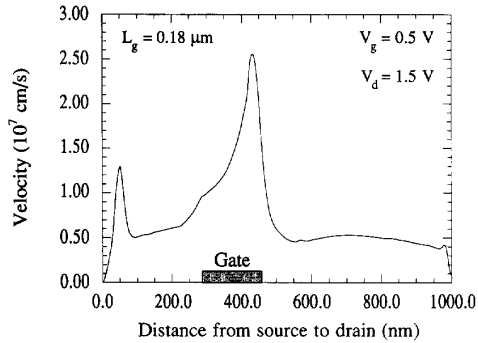


Fig. 10. Longitudinal velocity in the quantum well.

contact within a region much shorter than the gate length. In light of the quantum correction depending on the density change, the modification of the current by the quantum effects is understandable, since the electron density is high and the density change occurs over a short distance. As we expected, a similar density distribution across the conduction channel (to what we found in the GaAs/AlGaAs HEMT) is found in this device [14]. The electron densities with and without quantum potential included are plotted in Fig. 9, which shows the increase of the electron density in the channel when quantum potential is included.

Velocity overshoot, with a peak velocity of  $2.6 \times 10^7$  cm/s, was observed in the strained Si channel, and is very important

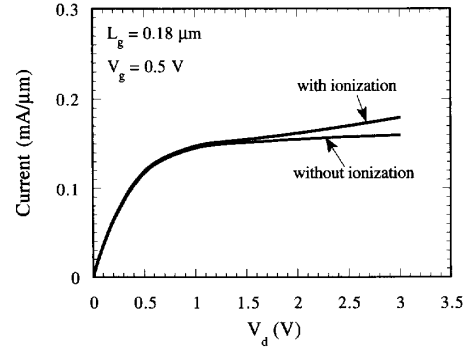


Fig. 11. I-V characteristics of the SiGe device, showing the impact ionization effect.

in achieving the transconductance observed. In Fig. 10, we plot the longitudinal velocity along the conduction channel in the quantum well. The bias condition in this case is  $V_g = 0.5$  V and  $V_d = 1.5$  V. The velocity overshoot in the gate region results in a peak velocity of  $2.6 \times 10^7$  cm/s. The overshoot is important in achieving the high transconductance for the device, for it introduces larger current flow along the quantum well. In other words, the velocity overshoot causes larger average velocity for the electron to travel through the channel. The first velocity peak in the plot is due to the model structure we used for the change of interface discontinuity [14], although it is not practical, it does suggest that the structure can increase the electron velocity between source and gate, which in turn will raise the average velocity through the device and enhance the device performance. By including the impact ionization rate from Monte Carlo simulation, we investigated the impact ionization effect on the device performance. Fig. 11 is the comparison of the drain current characteristics of the simulation for the fore mentioned SiGe device in the cases of with and without impact ionization, which shows that the generation effect on the I-V characteristics becomes large as drain voltage exceeds 1.5 V.

#### IV. CONCLUSIONS

In summary, we have studied the transport properties of an ungated Si/Si<sub>1-x</sub>Ge<sub>x</sub> system with an ensemble Monte Carlo technique and a Si/Si<sub>1-x</sub>Ge<sub>x</sub> FET structure with the QHE method. Since the strain at the heterointerface releases the degeneracy of the six-fold valleys in unstrained Si, electrons prefer to stay in the lowered valley normal to the interface, which reduces the intervalley scattering and transport is characterized by the smaller transverse mass. In the ungated structure, the velocity shows similar characteristics for strained Si for  $\Delta E \geq 0.1$  eV, although the electron energy increases with  $\Delta E$ . The electron mobility for strained Si is estimated to be  $4000 \text{ cm}^2/\text{Vs}$  at 300 K, and  $23000 \text{ cm}^2/\text{Vs}$  at 77 K, respectively. There is a slight increase in the saturation velocity compared with that of unstrained Si, at both 300 and 77 K. The overshoot peak velocity with a sudden application of the field 50 kV/cm is increased for larger  $\Delta E$ , and for  $\Delta E = 0.4$  eV, it is  $4.1 \times 10^7$  cm/s at 300 K and  $5.2 \times 10^7$  cm/s at 77 K, which

suggests great potential for future electron device applications. Device simulation predicts that the SiGe device performance falls into the same performance order of an AlGaAs/GaAs HEMT device. The simulated transconductance is comparable to the experimental results in [3]. The overshoot is important in achieving the high transconductance for the device, for it introduces larger current flow along the quantum well. Real space transfer generally occurs in the gate to drain region due to electrons gained higher energy and larger transverse electric field, but no negative differential conductance is observed in the device. With the potential good performance, the SiGe FET could become a very good electronic device in the future.

## APPENDIX

## MONTE CARLO MODEL FOR UNSTRAINED SI

The Monte Carlo model for the study of the transport properties in Si/Si<sub>1-x</sub>Ge<sub>x</sub> modulation-doped structure is based on the usual unstrained Si band-structure for three-dimensional electrons in a set of nonparabolic  $\Delta$  valleys [17]. Intravalley scattering within the same valley out of six  $\Delta$  valleys that are located about 85% of the way to the zone edge at  $X$ , is limited to acoustic phonon (and impurity) scattering, since the intravalley optical phonon scattering is forbidden by the symmetry [6], [18]. As for the intervalley phonons, there are two processes: one is referred to as the  $f$ -phonon process, which couples the (100) valley to the perpendicular valleys such that the (010) or (001) valleys, etc., and the other is referred to as a  $g$ -phonon process, which couples the (100) valley to the (-100) valley. The former is a normal process and the phonon momentum is  $\sqrt{2} \times 0.85\pi/a \sim 1.2\pi/a$  with  $a$  the lattice constant, and the latter is an umklapp process and the net phonon momentum is  $0.3\pi/a$ . By a group symmetry discussion, it has been shown that the zeroth-order low energy  $f$ - and  $g$ -phonon process are forbidden [6], [18]. Nevertheless, three zeroth-order  $f$ -phonons and three zeroth-order  $g$ -phonons with various energies are usually assumed [10].

We have taken into account this selection rule, and considered two high-energy  $f$ - and  $g$ -phonons and two low-energy  $f$ - and  $g$ -phonons in our simulation. The former two high-energy phonon scatterers are considered via the usual zeroth-order process [6], [10], and the latter two low-energy phonon scattering is forbidden so that they are treated via a first-order process, whose scattering rate  $\Gamma(k)$  for an electron with momentum  $k$  is given by [6], [18]

$$\Gamma(k) = \frac{2^{1/2} m^{*5/2} \Xi_0^2}{\pi \rho \hbar^5 \omega_0} [N_q (2E_k + \hbar\omega_0) \sqrt{E_k + \hbar\omega_0} + (N_q + 1) (2E_k - \hbar\omega_0) \sqrt{E_k - \hbar\omega_0} \cdot \theta(E_k - \hbar\omega_0)] \quad (\text{A1})$$

where  $m^*$  is the effective mass,  $\Xi_0$  is the first-order deformation potential,  $\rho$  is the mass density,  $\hbar\omega_0$  is the phonon energy,  $N_q$  is the number of phonons given by the Bose-Einstein distribution function,  $E_k$  is the electron kinetic energy, and  $\theta$  is a Heavyside function. The first term in the square bracket corresponds to absorption and the second term corresponds to

TABLE I  
PHONON MODEL FOR BULK UNSTRAINED SI

phonon	coupling constant	phonon energy
zeroth	$f$ -phonon	$8 \times 10^8$ eV/cm 59 meV
zeroth	$g$ -phonon	$8 \times 10^8$ eV/cm 63 meV
first	$f$ -phonon	2.5 eV 23 meV
first	$g$ -phonon	4.0 eV 18 meV

acoustic phonon 9.0 eV treated as elastic scattering

emission. The expression is modified when nonparabolicity is included, to

$$\Gamma(k) = \frac{2^{1/2} m^{*5/2} \Xi_0^2}{\pi \rho \hbar^5 \omega_0} \{N_q [\sqrt{s(1 + \alpha s)} E_k (1 + \alpha E_k) + s(1 + \alpha s)(1 + 2\alpha s)] + (N_q + 1) [\sqrt{t(1 + \alpha t)} E_k (1 + \alpha E_k) + t(1 + \alpha t)(1 + 2\alpha t)]\} \theta(E_k - \hbar\omega_0) \quad (\text{A2})$$

where the quantities  $s$  and  $t$  are defined by

$$s = E_k + \hbar\omega_0 \quad (\text{A3})$$

$$t = E_k - \hbar\omega_0 \quad (\text{A4})$$

and  $\alpha$  is the nonparabolicity parameter.

The energy dependence of the first-order interaction is  $E_k^{1.5}$  in the high-energy limit, in contrast with that of zeroth-order process  $E_k^{0.05}$  [6], [10]. As is obvious from this energy dependence, the first-order process is not important for low-energy electrons but gives a relevant contribution to the high-energy electrons. These first order processes involving low-energy phonons are important in achieving a smooth velocity saturation curve, especially at low temperatures [17]. The phonon energies and the coupling constants are unknown *a priori* and are determined so that the experimental velocity-field characteristics are consistently recovered. The choice of these parameters used in this paper is shown in Table I.

Impact ionization is treated with Ridley's soft impact-ionization model where the scattering rate for an electron with kinetic energy  $E_k$  is proportional to  $(E_k - E_{th})^2$  due to the convolution of valence- and conduction-band state densities, with ionization threshold energy  $E_{th}$  close to  $E_g$  [12]. In this model, the overlap integral of the cell-periodic part of the Bloch function, denoted by  $(I_c I_v)^2$  in [12], where  $I_c$  is the coupling between the original conduction-band electron and the generated electron and  $I_v$  is the coupling between the original electron and the generated hole, is not known *a priori* although it is expected to be on the order of unity. In practice, it is chosen so that the calculated velocity-field characteristics and ionization rate-field characteristics fit the experimental data. By assuming  $I_c I_v \sim 0.25$ , the impact ionization rate is  $\Gamma_{ion}(E) = 4.8 \times 10^{12} (E - E_{th})^2 / E_g^2$ , where the threshold energy  $E_{th}$  is assumed to be given by  $E_{th} = 1.18 E_g$ . This is a simple model extracting the essence of phenomena, and thus leaves some room for improvement. For example, the model does not explain the experimentally observed anisotropic directional dependence of impact ionization rate [19], although this can be recovered by assuming an anisotropic threshold  $E_{th}$  which is function of crystal orientation. It does not consider a quite likely phonon-assisted process, which may alter the

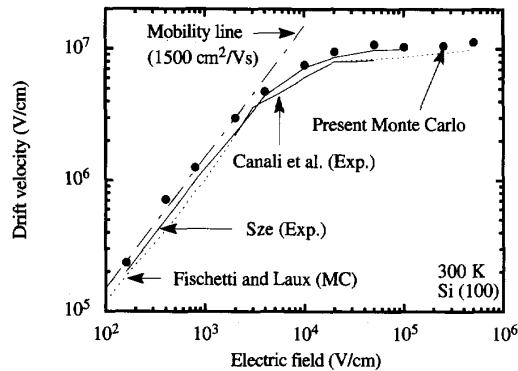


Fig. 12. Velocity-field characteristics of unstrained Si at 300 K.

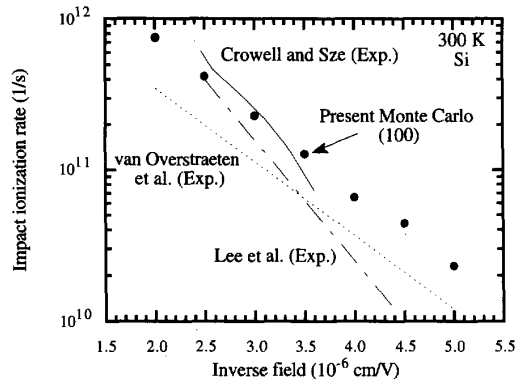


Fig. 13. Impact ionization rate as a function of inverse electric field in unstrained Si at 300 K.

requirement of momentum conservation law for carriers near the threshold, and alter the energy dependence of the ionization scattering rate [15]. In spite of these points, we believe the essential feature of the impact ionization is described in this model, and the model is applicable to the modeling of the transport in  $\text{Si}/\text{Si}_{1-x}\text{Ge}_x$ .

All the simulation results discussed below are for electrons in unstrained bulk Si at 300 K, with the electric field applied in the (100) direction. Fig. 12 shows the velocity-field characteristics denoted by dots. Some curves are shown for reference, a straight line corresponding to the mobility value of  $1500 \text{ cm}^2/\text{Vs}$  [11], two experimental curves by Sze [11] and Canali *et al.* [20], a Monte Carlo curve by Fischetti and Laux [15] obtained with a full-conduction-band model. Agreement is good. Fig. 13 shows the impact-ionization rate as a function of inverse electric field. Three experimental curves are shown, by Crowell and Sze [21], by van Overstraeten and DeMan [22], and by Lee *et al.* [23]. These experimental curves exhibit differences, and our ionization rate lies within the experimental error of them.

Fig. 14(a) shows the population and Fig. 14(b) shows the distribution function defined for several electric field values. It is clearly seen that the distribution function has a sharp downward convex part for small energy values, and this trend is more prominent with increasing field. This is due to the

impact ionization. If impact ionization occurs, the electron loses energy equal to  $E_g$  and has a small energy, and the generated electron-hole pair is discarded from the simulation. Thus many electrons are located at low energy due to impact ionization, and this causes the characteristic curve in the distribution function at small energies. In fact, the ratio of electrons above the impact-ionization threshold energy  $E_{th}$  (1.31 eV) is  $3.9 \times 10^{-2}$ , 8.1, and 35% for  $1 \times 10^5$ ,  $2.5 \times 10^5$ , and  $5 \times 10^5 \text{ V/cm}$ , respectively. Although the impact ionization is treated in a quite simple manner in the simulation, an accumulation of low energy electrons in an inevitable conclusion of impact ionization as long as original electrons lose most of their energy in the process. The distribution function changes its gradient at high energies due to the influence of intervalley scattering, which was reported before [10], [16]. Around  $E = 2.38 \text{ eV}$ , the  $\Delta$ -valley conduction band has a local maximum [15] and our simple nonparabolic-band model may not be appropriate. The ratio of electrons above this energy is  $1.8 \times 10^{-4}$ , 0.21m and 5.1% for  $1 \times 10^5$ ,  $2.5 \times 10^5$ , and  $5 \times 10^5 \text{ V/cm}$ , respectively, and we can safely neglect the complicated conduction-band structure for fields smaller than  $5 \times 10^5 \text{ V/cm}$ , if we are not interested in effects arising from the tail (for example, we cannot expect to model oxide injection with this model). Fig. 15 shows the energy-field characteristics. This is not experimentally measurable directly, but still can be compared with other existing Monte Carlo results for consistency. Two Monte Carlo curves by Canail *et al.* with a parabolic-band model [28] and Fischetti *et al.* with a full-conduction-band model [15] are shown and our result agrees well with theirs.

Our Monte Carlo model, like other models [10], does not include the  $L$  valley directly, which merges at  $E = 1.05 \text{ eV}$ . Full-conduction-band Monte Carlo models have been proposed which use a realistic state density function determined by the shape of the band and include  $\Delta-L$  and  $L-L$  intervalley scattering [15], [19], in addition to the usual  $\Delta-\Delta$  intervalley scattering that we also adopted here. Our model has effectively included the influence of  $L$  valley in the values of phonon energies and coupling constants, and shows practically the same results as those of the full-conduction-band model as demonstrated above. There are discussions about the validity of applying a semiclassical Fermi golden-rule picture to the  $L-L$  or  $\Delta-L$  high-energy intervalley scattering under a strong electric field, where an electron may be accelerated by the field during the collision process (intracollisional field effect), and the electron energy may not be a well defined single value because of collision broadening [24]. Many attempts have been made to study these effects based on a field-theoretical approach [24], but no common prescription for the treatment of these effects has been established at this stage. In this sense, if the  $L$  valley is treated semiclassically with the Fermi golden rule, it is already a significant approximation, and this problem is left as an open question for future study. It has to be stressed that the full-conduction-band Monte Carlo model including the  $L$  valleys is preferable but as long as there is no phonon-scattering model to include these quantum effects in high fields, our simple nonparabolic-band Monte Carlo model is practically useful.

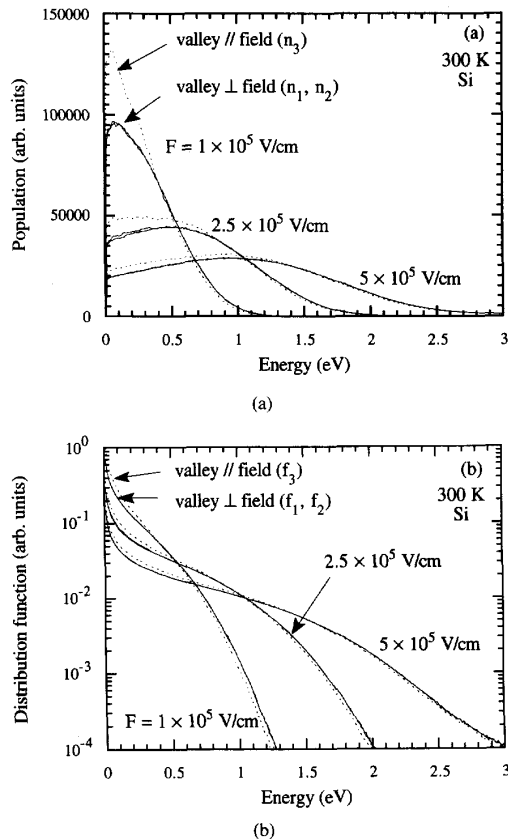


Fig. 14. (a) Population and (b) distribution function in unstrained Si at 300 K for  $1 \times 10^5$ ,  $2.5 \times 10^5$ , and  $5 \times 10^5$  V/cm.

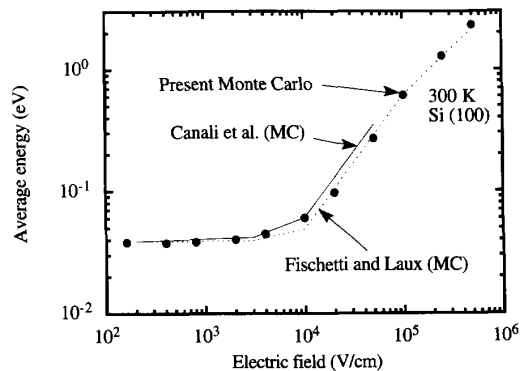


Fig. 15. Energy-field characteristics of unstrained Si at 300 K.

The following remarks have to be made on the choice of some unknown parameters such as phonon energies, coupling constants, and overlap integrals. First, our choice is just one example out of many possibilities and we do not exclude other possibilities. The only way to judge how the choice is reasonable is to compare the results with the experimental velocity-field characteristics and impact ionization rate. As long as they are well recovered, the different choices of parameters should not be excluded. Second, the impact-

ionization scattering rate is rather insensitive to the value of the overlap integrals  $I_c I_v$  of the cell-periodic part of the Bloch function, or the numerical coefficient of the quadratic function of the electron kinetic energy  $E_k$  as  $(E_k - E_{th})^2$ , as was reported before [19]. The appropriate value of  $I_c I_v$  is closely connected to the phonon model used in the simulation (the number of phonon modes, the phonon energies, the coupling constants, whether the first-order process is considered or not) and cannot be simply compared with other Monte Carlo models if the phonon model is different. Third, although there is some ambiguity in the physical modeling and the choice of parameters, our conclusions on the high-temperature transport properties for Si/Si<sub>1-x</sub>Ge<sub>x</sub> that are directly based on the bulk Si Monte Carlo simulation—enhanced mobility and slightly faster saturation velocity at 77 and 300 K, large velocity overshoot a few times faster than the saturation velocity in both a bulk structure and a device structure—are not affected even if a different physical model or a different choice of parameters are adopted.

#### ACKNOWLEDGMENT

The authors are grateful to P. Bordone for useful discussions.

#### REFERENCES

- [1] Y. J. Mii, Y. H. Xie, E. A. Fitzgerald, Don Monroe, F. A. Thiel, and E. B. Weir, "Extremely high electron mobility in Si/Si<sub>1-x</sub>Ge<sub>x</sub> structures grown by molecular beam epitaxy," *Appl. Phys. Lett.*, vol. 59, pp. 1611–1613, 1991.
- [2] D. Többen, F. Schäffler, A. Zrenner, and G. Abstreiter, "Magnetotransport measurements and low-temperature scattering times of electron gases in high-quality Si/Si<sub>1-x</sub>Ge<sub>x</sub> heterostructures," *Phys. Rev. B*, vol. 46, pp. 4344–4347, 1992.
- [3] K. Ismail, B. S. Meyerson, S. Rishton, J. Chu, S. Nelson, and J. Nocera, "High-transconductance n-type Si/SiGe modulation-doped field-effect transistor," *IEEE Trans. Electron Device Lett.*, vol. 13, pp. 229–231, 1992.
- [4] G. Abstreiter, H. Brugger, T. Wolf, H. Jorke, and H. J. Herog, "Strain-induced two-dimensional electron gas in selectively doped Si/Si<sub>x</sub>Ge<sub>1-x</sub> superlattices," *Phys. Rev. Lett.*, vol. 54, pp. 2441–2444, 1985; R. People, "Physics and applications of Ge<sub>x</sub>Si<sub>1-x</sub>/Si strained-layer heterostructures," *IEEE J. Quantum Electron.*, vol. 22, pp. 1696–1710, 1986.
- [5] J.-R. Zhou and D. K. Ferry, "Simulation of ultra-small GaAs MESFET using quantum moment equations," *IEEE Trans. Electron Devices*, vol. 39, pp. 473–478, 1992.
- [6] D. K. Ferry, *Semiconductors*. New York: Macmillan, 1991.
- [7] H. Miyata, T. Yamada, and D. K. Ferry, "Electron transport properties of a strained Si layer on a relaxed Si<sub>1-x</sub>Ge<sub>x</sub> substrate by Monte Carlo simulation," *Appl. Phys. Lett.*, vol. 62, pp. 2661–2663, 1993.
- [8] T. Ando, A. B. Fowler, and F. Stern, "Electronic properties of two-dimensional systems," *Rev. Mod. Phys.*, vol. 54, pp. 437–672, 1982.
- [9] M. M. Rieger, Diplomarbeit, Technical University München, Germany, 1991, unpublished.
- [10] C. Jacoboni and R. Reggiani, "The Monte Carlo method for the solution of charge transport in semiconductors with applications to covalent materials," *Rev. Mod. Phys.*, vol. 55, pp. 645–705, 1983.
- [11] S. M. Sze, *Physics of Semiconductor Devices*. New York: Wiley, 1981.
- [12] B. K. Ridley, "Soft-threshold lucky drift theory of impact ionization in semiconductors," *Semicond. Sci. Technol.*, vol. 2, pp. 116–122, 1987.
- [13] B. K. Ridley, "Reconciliation of the Conwell-Weisskopf and Brooks-Herring formulae for charged impurity scattering in semiconductors: Third body interference," *J. Phys. C: Solid State Phys.*, vol. 10, pp. 1589–1593, 1977; T. G. Van de Roer and F. P. Widdershoven, "Ionized scattering in Monte Carlo calculations," *J. Appl. Phys.*, vol. 59, pp. 813–815, 1986.

- [14] J.-R. Zhou and D. K. Ferry, "Simulation of quantum effects in ultrasmall HEMT devices," *IEEE Trans. Electron Devices*, vol. 40, pp. 421-427, 1993.
- [15] M. V. Fischetti and S. E. Laux, "Monte Carlo analysis of electron transport in small semiconductor devices including band-structure and space-charge effects," *Phys. Rev. B*, vol. 38, pp. 9721-9745, 1988; see also M. V. Fischetti, "Monte Carlo simulation of transport in technologically significant semiconductors of the diamond and zinc-blende structures-Part I: homogeneous transport," *IEEE Trans. Electron Devices*, vol. 30, pp. 634-649, 1991.
- [16] W. Fawcett and E. G. S. Paige, "Negative differential mobility of electrons in germanium: A Monte Carlo calculation of the distribution function, drift velocity and carrier population in the  $< 111 >$  and  $< 100 >$  minima," *J. Phys. C.: Solid St. Phys.*, vol. 4, pp. 1801-1821.
- [17] P. Luglie and D. K. Ferry, "Effect of electron-electron scattering on Monte Carlo studies of transport in submicron semiconductor devices," *Physica*, vol. 117B, pp. 251-253, 1983; "Effect of electron-electron and electron-plasmon interactions on hot carrier transport in semiconductors," *Physica*, vol. 129B, pp. 532-536, 1985; "Electron-electron interaction and high field transport in Si," *Appl. Phys. Lett.*, vol. 46, pp. 594-596, 1985; "Dynamical screening of hot carriers in semiconductors from a coupled molecular-dynamics and ensemble Monte Carlo simulation," *Phys. Rev. Lett.*, vol. 56, pp. 1295-1297, 1986.
- [18] D. K. Ferry, "First-order optical and intervalley scattering in semiconductors," *Phys. Rev. B*, vol. 14, pp. 1605-1609, 1976; W. Siegel, A. Heinrich, and E. Ziegler, "Electron and hole mobility in  $ZnSiP_2$ ," *Phys. Stat. Sol.*, vol. a 35, pp. 269-279, 1976; B. K. Ridley, *Quantum Processes in Semiconductors*. Oxford: Clarendon, 1982.
- [19] H. Shichijo and K. Hess, "Band-structure-dependent transport and impact ionization in GaAs," *Phys. Rev. B*, vol. 23, pp. 4197-4207, 1981.
- [20] C. Canali, C. Jacoboni, F. Nava, G. Ottaviani, and A. Alberigi-Quaranta, "Electron drift velocity in silicon," *Phys. Rev. B*, vol. 12, pp. 3318-3329, 1975.
- [21] C. R. Crowell and S. M. Sze, "Temperature dependence of avalanche multiplication in semiconductors," *Appl. Phys. Lett.*, vol. 9, pp. 242-244, 1966.
- [22] R. van Overstraeten and H. DeMan, "Measurement of the ionization rates in diffused silicon p-n junctions," *Solid-State Electron.*, vol. 13, pp. 583-608, 1970.
- [23] C. A. Lee, R. A. Logan, R. L. Batdorf, J. J. Kleimack, and W. Wiegman, "Ionization rates of holes and electrons in silicon," *Phys. Rev.*, vol. 134, pp. A761-A773, 1964.
- [24] It is impossible to cover this topic: as a review, see *Quantum Transport in Semiconductors*, C. Jacoboni, L. Reggiani, and D. K. Ferry, Eds. New York: Plenum, 1992. The quantum mechanical treatment of transport phenomena are studied in K. K. Thornber and R. P. Feynman, "Velocity acquired by an electron in a finite electric field in a polar crystal," *Phys. Rev. B*, vol. 1, pp. 4099-4114, 1970; J. R. Barker and D. K. Ferry, "Self-scattering path-variable formation of high field, time-dependent quantum kinetic equation for semiconductor transport," *Phys. Rev. Lett.*, vol. 42, pp. 1779-1781, 1979; W. Hänsch and G. D. Mahan, "Transport for many-particle system," *Phys. Rev. B*, vol. 28, pp. 1902-1922, 1983; Y.-C. Chung, D. Z.-Y. Ting, J. Y. Tang, and K. Hess, "Monte Carlo simulation of impact ionization in GaAs including quantum effects," *Appl. Phys. Lett.*, vol. 42, pp. 76-78, 1983; G. D. Mahan, "Electron transport in solids," *Phys. Rep.*, vol. 110, pp. 321-331, 1984; A.-P. Jauho and J. W. Wilkins, "Theory of high-electric-field quantum transport for electron-resonant impurity systems," *Phys. Rev. B*, vol. 29, pp. 1919-1938, 1984; M. V. Fischetti and D. J. DiMaria, "Quantum Monte Carlo simulation of high-field electron transport: an application to silicon dioxide," *Phys. Rev. Lett.*, 55, pp. 2475-2478, 1985; R. Bertoncini, A. M. Kriman, and D. K. Ferry, "Airy coordinate technique for nonequilibrium Green's function approach to high-field quantum transport," *Phys. Rev. B*, vol. 41, pp. 1390-1400, 1990.



**Toshishige Yamada** (S'91-M'93) received the B.S. and M.S. in physics from the University of Tokyo, Tokyo, Japan, in 1981 and 1983, respectively, and Ph.D. in Electrical Engineering from Arizona State University in 1992.

From 1983 to 1988, he was with NEC Microelectronics Research Laboratories, Kawasaki, Japan, where he was engaged in the research of Josephson latch circuits, and later that of semiconductor transport simulation. He joined the Electrical Engineering Department of Arizona State University as

a graduate research associate in 1988, and graduated with the dissertation on the molecular-dynamics Monte Carlo study of the transport properties of lateral surface superlattices under Professor D. K. Ferry in 1992. Following the graduation, he has been a postdoctoral faculty associate of the same institution, in charge of the research of semiconductor transport simulation.

Dr. Yamada is a member of Sigma Xi, Phi Kappa Phi, and the American Physical Society.



**Jing-Rong Zhou** (S'87-M'92) received the B.S. degree in applied physics and M.S. degree in electrical engineering from China, and the Ph.D. degree in electrical engineering from Arizona State University in 1982, 1985, and 1991, respectively.

He worked on optical fiber sensor research and optical fiber theory from 1985 to 1986. He is currently a Research Analyst in the Center for Solid State Electronics Research at Arizona State University, working on the modeling and simulation of semiconductor devices. His research interests

include semiconductor device and process simulation, device characterization and device physics, semiconductor transport theory, and quantum transport.

Dr. Zhou is a member of Sigma Xi.

**H. Miyata**, photograph and biography not available at time of publication.



**David K. Ferry** (S'61-M'62-SM'72-F'86) received the Ph.D. degree from the University of Texas at Austin.

He is currently Regents' Professor of Electrical Engineering at Arizona State University, Tempe, AZ. He has worked in the area of semiconductor transport and semiconductor devices for more than 25 years, and is recognized for both his experimental and theoretical contributions in these areas. During his career, he was awarded a fellowship at the Boltzmann Institute of Solid State Physics in Vienna and has held positions at Texas Tech University, Colorado State University, and the Office of Naval Research. In addition, he has organized several NATO Advanced Study Institutes in the area of semiconductors. He is author and coauthor of over 300 scientific works.

Dr. Ferry is a Fellow of the American Physical Society.